ORIGINAL

CrossMark

Flame behavior and thermal structure of combusting plane jets with and without self-excited transverse oscillations

Rong Fung Huang [1] · Reuben Mwanza Kivindu [1] · Ching Min Hsu [2]

Abstract

The flame behavior and thermal structure of combusting plane jets with and without self-excited transverse oscillations were investigated experimentally. The transversely-oscillating plane jet was generated by a specially designed fluidic oscillator. Isothermal flow patterns were observed using the laser-assisted smoke flow visualization method. Meanwhile, the flame behaviour was studied using instantaneous and long-exposure photography techniques. Temperature distributions and combustion-product concentrations were measured using a fine-wire type R thermocouple and a gas analyzer, respectively. The results showed that the combusting transversely-oscillating plane jets had distributed turbulent blue flames with plaited-like edges, while the corresponding combusting non-oscillating plane jet had laminar blue-edged flames in the near field. At a high Reynolds number, the transversely-oscillating jet flames were significantly shorter and wider with shorter reaction-dominated zones than those of the non-oscillating plane jet flames. In addition, the transversely-oscillating combusting jets presented larger carbon dioxide and smaller unburned hydrocarbon concentrations, as well as portrayed characteristics of partially premixed flames. The non-oscillating combusting jets presented characteristics of diffusion flames, and the transversely-oscillating jet flame had a combustion performance superior to its non-oscillating plane jet flame counterpart. The high combustion performance of the transversely-oscillating jets was due to the enhanced entrainment, mixing, and lateral spreading of the jet flow, which were induced by the vortical flow structure generated by lateral periodic jet oscillations, as well as the high turbulence created by the breakup of the vortices.

Keywords Plane jet flame · Flame behavior · Fluidic oscillation · Flow control

Nomenclature

b	Width of exit slots of fluidic oscillator, 0.5 mm.
C_{CO}	Concentrations of carbon monoxide.
C_{CO2}	Concentrations of carbon dioxide.
C_{O2}	Concentrations of oxygen.
C_{UHC}	Concentrations of unburned hydrocarbons.
d	Width of fluidic oscillator passageway, 1 mm.
d_p	Width of jet exit, 11 mm.
h	Offset distance from crescent origin to virtual vertex of target blockage, 2 mm.
H_f	Flame length, m.
l	Length of deflection plates, 5.5 mm.
Q_j	Volumetric flow rate of fluid jet measured by rotameter, m^3/s.
R	Radius of crescent profile of the target blockage, 4.5 mm.
Re_j	Reynolds number of fuel jet flow, $= u_j d_p / \nu_j$.
s	Span length of burners, 36 mm.
T	Temperature, °C.
t	Evolution time, s.
t^*	Non-dimensional evolution time, $= t u_c / d_p$.
UHC	Unburned hydrocarbons.
u_c	Average jet velocity at the nozzle inlet, m/s.
u_j	Average exit velocity of plane jet, $= Q_j / (s d_p)$, m/s.
u'	Root mean square of fluctuating velocity, m/s.
w	Cross-stream distance between exit slots of fluidic oscillator, 16.4 mm.
w_b	Downstream width of target blockage, 15 mm.
W_b	Overall width of burners, 36 mm.

✉ Rong Fung Huang
  rfhuang@mail.ntust.edu.tw

1 National Taiwan University of Science and Technology, Taipei 10672, Taiwan, Republic of China

2 National Formosa University, Yunlin County 63246, Taiwan, Republic of China

W_f Flame width, m.

x, y, z Coordinates in lateral, span, and axial directions fixed at centre of burner exit plane.

θ Deflection angle of deflection plates measured from horizontal axis, 30 degrees.

ν_j Kinematic viscosity of jet fluid, m^2/s

1 Introduction

For decades, plane jets have been studied due to their wide range of applications in industrial mixing processes, power generation, propulsion, heat transfer, and environmental control operations [1–5]. Investigations of planar jets, turbulent jets, and impinging jets have shown the existence of coherent structures and counter-rotating vortex pairs on alternate sides of the jets, which at times may merge [1, 2, 6–8]. The resulting flow structures, consequential transport phenomena, interactions, and merging of different-sized vortices in the mixing layer due to flow modifications improved entrainment, lateral spreading, and the jet axial momentum decay rate. However, the global performance of plane jet applications in combustion and mixing were challenged by a strong axial momentum, low lateral spread rates, and poor entrainment and mixing abilities.

The performance of natural plane jets in mixing and combustion may be improved by flow-control techniques, such as jet impingement, varying the shape at the nozzle exit, tripping the jet, acoustic excitation, swirl flow, jet fluidic oscillation, bluff bodies, jet injection into V-gutters, injection of an external mass, and passing the jet over a cavity [6, 8–20]. The nozzle geometry and aspect ratio (AR) did influence entrainment, mean velocity, and lateral spread rates [3–5, 21]. Bluff bodies were used to hold and stabilize flames close to the nozzle. The rationale behind the use of bluff bodies was the creation of shear layers, vortex shedding, and recirculation in the wake region to enhance fuel-air mixing and the mixing of fresh gases with hot gases, particularly for turbulent non-premixed jets. Bluff bodies were of diverse shapes, such as flat plates, cylinders, wedges, V-gutters, and slit V-gutters [22–25]. Research has shown the existence of low-frequency vortex shedding and high-frequency shear-layer instabilities in the wake of V-gutters [26]. The Coanda effect was employed to re-design the conventional V-gutter into a slit V-gutter and a V-shaped fluidic oscillator, resulting in stable self-sustained periodic fluidic oscillations and smaller turbulence length scales [9, 10]. Transverse oscillations in a plane jet could be induced in the wake region of a V-shaped fluidic oscillator by installing two short deflection plates near the exits of the alternatively pulsating issued jets [11]. This would result in significant axial momentum dispersion over a short axial distance and large turbulence intensities in the merged flow, thereby improving plane jets significantly. These characteristics are important in the practical applications of combustion, heat transfer, and mixing.

The non-premixed combustion of a free fuel jet issuing into quiescent air is well known to be a diffusion-limited process, as the fuel in the jet and the air are transported toward each other by molecular and convective diffusion processes, which are slower compared to the chemical reaction rate. Hence, the use of a transversely-oscillating fuel jet may result in the improved dispersion of the fuel jet and mixing rate, as transverse oscillations in a plane jet create counter-rotating vortices in the near-wake region and large turbulence intensities [10, 11], which enhance the transportation and mixing of the species. The faster mixing of fuel and air promotes better combustion rates and efficiencies that transform into fuel savings.

A V-shaped fluidic oscillator was installed at the exit of a plane fuel jet to investigate the effects of pulsating jets on flame behavior [27–29]. When compared to a non-pulsating plane jet flame, the pulsating jet flame improved with a 45% length reduction and a 40% width gain. The pulsating jet flames also presented higher and wider transverse temperature distributions than those of the non-pulsating ones. However, at higher flow rates, the flame lifted and had two flame branches near the base that merged higher up. The gap between the divergent flames may have negative effects on the combustion rate and efficiency.

This study investigated the flame behavior and thermal structure of combusting transversely-oscillating plane jets created by merging alternatively pulsating fuel jets issued from a fluidic oscillator. Two short deflection plates were installed near the exits of the fluidic oscillator to deflect the alternately pulsating fuel jets toward the central axis, where they merged and induced transverse oscillations [11]. A non-oscillating plane jet burner with a geometry and sizes corresponding to the transversely-oscillating plane jet burner was also designed and tested for comparison purposes.

2 Experimental apparatus and methods

2.1 Burner configurations and setup

A fluidic oscillator burner that can induce self-excited transverse jet oscillations was used in this study, as shown in Fig. 1a. It was developed by Huang and Chang [11] to investigate the periodic transverse oscillation properties, flow characteristics, and dispersion and mixing enhancement of the jets. The fuel gas was passed through the flow straighteners, a nozzle with a fifth-order polynomial profile, and a narrow rectangular channel of width $d = 1$ mm, and it was then injected into the fluidic oscillator cavity. The cavity was formed by two side blocks and a top target block. The top target block had a crescent surface of radius $R = 4.5$ mm facing the jet inlet. The two side blocks and the target block
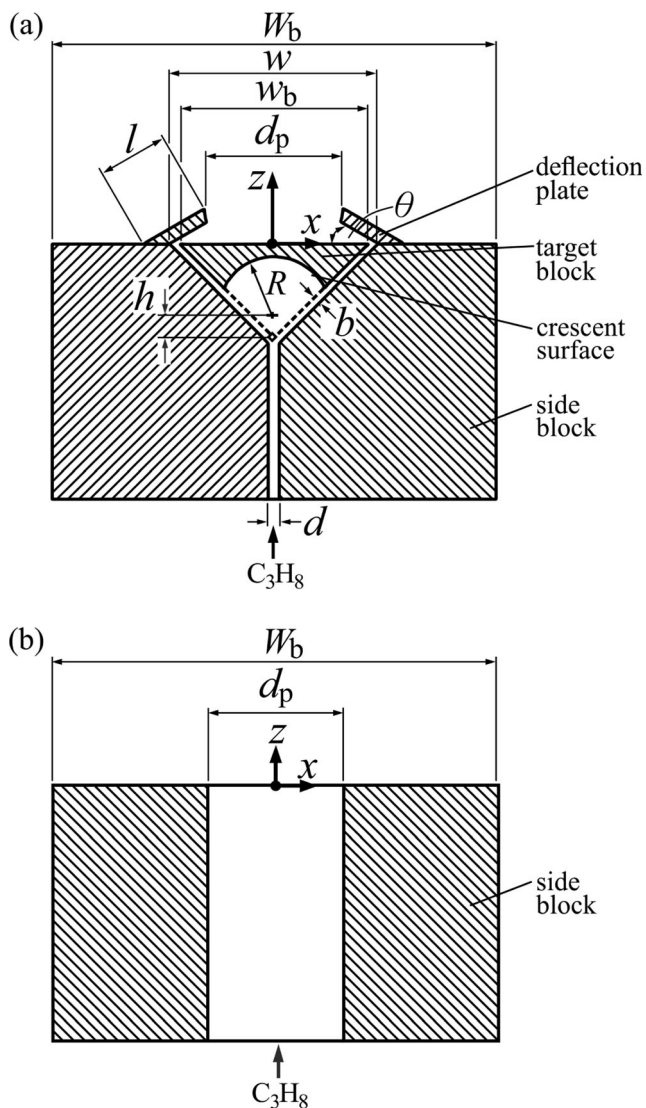
Fig. 1 Experimental setups. (**a**) Fluidic oscillator burner, (**b**) plane jet burner

were made of stainless steel. The target block had a downstream width of $w_b = 15$ mm, while the passages between the side blocks and the target block had a width of $b = 0.5$ mm. The center of the radius of the crescent surface of the target block was offset from the center of the jet exit at the inlet of the fluidic oscillator cavity by a height of $h = 2$ mm. With the optimized design, the jet impinging the crescent surface of the top target block could swing back and forth transversely in the cavity and eject alternately out of the exits of the side passages on the top plane of the device. To merge the self-excited pulsing jets that issued alternately out of the top exits to form a transversely-oscillating plane jet, two stainless steel deflection plates of length $l = 5.5$ mm were installed at $\theta = 30°$ from the horizontal axis, as shown in Fig. 1a. The width of the opening between the tips of the two deflection plates, from where the merged jet issued, was $d_p = 11$ mm. The overall set-up

width was $W_b = 36$ mm, and the span of the burner was $s = 36$ mm, while the AR of the transversely-oscillating jet was $s/d_p = 3.27$. The three-dimensional (3-D) flow may appear near the ends of the device span [21]; therefore, the experiments were performed at the central plane of the flow field to alleviate the influence of the 3-D effects. The jet Reynolds number was defined as $Re_j = u_j d_p / v_j$, where u_j is the jet velocity at the opening between the tips of the two deflection plates, d_p is the width of the jet exit at the opening between the tips of the two deflection plates, and v_j is the kinematic viscosity of the jet fluid. The coordinate system (x, y, z) referred to in the study was attached to the central location of the downstream surface of the target block.

For comparison, a plane jet burner, made of stainless steel, was designed, as shown in Fig. 1b. The plane jet burner was adapted such that its channel width at the exit and overall width were equivalent to d_p and W_b in Fig. 1a, respectively. The plane jet burner was subjected to similar flow conditioning as that of the fluidic oscillator burner before emerging at the burner exit. Because the fuel flow rates were maintained, corresponding values of Re_j for the fluidic oscillator burner were used. The experiments were performed at times when there were minimal activities in the laboratory, and wire mesh was used as a guard to avoid interference with the experimental conditions.

The fuel gas used was commercial-grade propane (95.0% C_3H_8, 3.5% C_2H_6, and 1.5% C_4H_{10}) supplied from a propane pressure tank. Flow rate metering was achieved with a pressure regulator, needle valve, and a calibrated rotameter, which were installed in the piping system. The rotameter was calibrated using a micro pressure calibration system (composed of a high-precision pressure transducer) installed in the laboratory. The jet bulk velocity u_j—based on the fuel flow rate—was defined as the flow rate Q_j (measured by a calibrated rotameter) divided by the cross-sectional area of the opening between the tips of the two deflection plates. The fuel jet emerging out of the burner port issued into quiescent air, where the mixing and introduction of the air into the combustion zone are dependent on molecular and convective diffusions and the entrainment induced by the vortical flow structures in the gaseous fuel jets. In this study, fuel jet flows in the range of $0 \leq Re_j \leq 1200$ are considered low Reynolds numbers, while fuel jet flows in the range of $1200 < Re_j < 2500$ are high Reynolds numbers. The temperature of the environmental air was 24–27 °C, and the corresponding air density was 1.199–1.176 kg/m^3 at 1 atm. At 25 °C, the value of the fuel jet density was 1.870 kg/m^3, while the values of the air and fuel jet kinematic viscosities were 1.547×10^{-5} and 4.395×10^{-6} m^2/s, respectively. Before starting the experiments, a non-directional hot-wire anemometer was used to detect the environmental draft velocities in the test room. The measured draft velocities were less than 0.1 m/s. Investigations were done by varying the jet velocity of the fuel.

2.2 Flow visualization

The laser-assisted smoke flow visualization technique was used to reveal the isothermal flow patterns downstream of the burners. The flow patterns are considered isothermal because the flow process is non-reacting; hence, the temperature remains constant during the visualization process. The smoke was generated by a homemade smoke generator that vaporized liquid kerosene oil using an electrically heated spiral wire that was partly immersed in an oil pot. A continuous greenlight laser sheet was used to illuminate the smoke flow patterns in the downstream wake region of the burners. A highspeed charge-coupled device camera (Model Xstream Version^{Tm} XS-4, IDT Inc.) installed perpendicular to the green-light laser sheet was used to record the illuminated smoke patterns. The instantaneous flow patterns were captured with the camera exposure time set at 250 μs and at a frame rate of 200 fps.

2.3 Detection of jet oscillation and turbulence fluctuations

A homemade, constant-temperature, one-component hotwire anemometer was used to detect the turbulence fluctuations and oscillation frequencies of the jet under nonreacting conditions. The hot-wire anemometer was a TSI 1210-T1.5 single-wire probe with the original tungsten wire replaced with a platinum wire of 5 μm in diameter and 1.5 mm in length. Because the vortical flows travelled downstream, the single-wire probe was arranged in an "end-flow" fashion to detect the axial velocities. The hot-wire anemometer was calibrated in a wind tunnel using a Pitot tube associated with a high-precision electronic pressure transducer. For flow velocities lower than the lower limit of the Pitot tube measurement, a fourthorder polynomial curve was employed to fit the calibration data down to a null velocity. An analog low-pass filter was connected to the output signals of the hot-wire anemometer. The cut-off frequency of the low-pass filter was set at 6 kHz, which was significantly higher than the highest expected frequency of jet oscillation (approximately 120 Hz) and which covered the energycontaining and inertial ranges of turbulence. The sampling rate and elapse time of the data acquisition system were set to 10,000 samples per second and 3 s, respectively. The output signals of the hot-wire anemometer were fed simultaneously to a fast Fourier transform analyzer and a high-speed personal computer-based data acquisition system for analysis. The uncertainty of the velocity measurement in the low velocity range was estimated using the calibration curve to be approximately ±3.5% of a reading. The frequency detection uncertainty was estimated to be approximately ±0.8% of a reading.

2.4 Flame visualization

To visualize the flame behavior, both short- and longexposure flame images were captured using a digital camera (Nikon Corp., model D3200) that had an exposure time range of 1/4000–30 s. The camera used was a single-lens reflex digital camera with an effective angle of view of 1.5 × lens focal length. Flame images were captured with the camera facing the y-direction. Preliminary experiments were performed by capturing several images at different exposure times to determine the suitable exposure time for the flame behavior investigation. Near-field flame images were acquired at a short exposure time of 1 ms, while far-field flame images were acquired at a long exposure time of 2 s. The flame length, H_f, was defined as the vertical distance measured from the level $z = 0$ to the upper boundary of the flame tip. Meanwhile, the flame width, W_f, at a given axial level was defined as the horizontal distance between the left and right boundaries of the flame [22, 29, 30]. The flame length and width data were acquired by averaging over 40 and 25 longexposure images, respectively. Therefore, the flame lengths and widths were obtained equivalently based on the images, of 80-s and 50-s exposure times, respectively. The standard errors of the mean were estimated to be within ±3.75 and ±1.65 mm for the flame length and width, respectively.

2.5 Temperature measurements

Flame temperature measurements were made using a homemade type R thermocouple probe. The detecting probe consisted of a 125-μm diameter wire and a 175-μm diameter spark-welded bead. The probe wires were housed in a twoholed ceramic tube of diameter 1.8 mm with the probe measuring bead protruding 15 mm from the ceramic tube. The ceramic tube was fastened securely in an L-shaped stainless steel tube to ensure probe rigidity. The probe assembly was positioned in the test section by a step motor-driven traversing mechanism with a minimum step resolution of 10 μm. Temperature measurements were carried out with a data logger (Yokogawa Corp., model MX100-E-1D). For each point measurement, data were acquired at a sampling frequency of 2 Hz. The arithmetic averages were obtained over a fixed period of 4.5 min.

2.6 Combustion-product concentration measurements

The combustion-product concentrations were measured using a portable multi-gas analyzer (NOVA Analytical Systems Inc., Model 7466 K), which was able to analyze oxygen (O_2), carbon dioxide (CO_2), carbon monoxide (CO), and unburnt hydrocarbon (UHC) simultaneously. The concentrations for CO, CO_2, and UHC were detected and measured by a single non-

dispersive infrared detector, while O_2 was detected by a long-life electrochemical sensor. The analyzer's full scales for measuring O_2, CO, and CO_2 were 25%, 10%, and 20%, respectively, while the available range for UHC was 0–20,000 ppm. The gas analyzer had a response time of 8–10 s. An L-shaped stainless steel tube with a 3-mm outer diameter and a 2.4-mm inner diameter was used as the concentration probe. The combustion gases were drawn continuously through the probe, a dehumidifying system, and a soot remover, and they were then directed into the gas analyzer. To ensure the minimum suction influence on the flow and flame, an average suction rate of 850 cm^3/min was established from a preliminary test. Long-term data stabilized within a period of 5 min were recorded for each point sampled. The probe was positioned in the test section using a step motor-driven 3-D traversing mechanism with a minimum step resolution of 10 μm. The sampling of the combustion product concentrations was done at various axial stages (z/d_p = 0.7, 4, and 20) with a traversing step of 2 mm.

3 Results and discussion

3.1 Flow characteristics of transversely-oscillating jets

Figure 2 shows the instantaneous isothermal flow patterns downstream of the flow exit of the fluidic oscillator burner shown in Fig. 1a. The jet Reynolds number is Re_j = 121, and the jet fluid is air. The dimensionless time t^* marked on the pictures is defined as $t^* = tu_c/d_p$, where t is the evolving time starting from the beginning of a cycle and u_c is the average jet velocity at the nozzle inlet. In Fig. 2a (t^* = 0), two counter-rotating vortices appear in the small cavity enclosed by the deflection plates. A four-way saddle exists at the vertex of the vortex pair. A jet evolves from the four-way saddle and ejects toward the upper-left direction. This flow pattern is formed due to the merging of the alternately bifurcated jets issued from the passageways of the fluidic oscillator [11]. In Fig. 2b (t^* = 1.66), the left vortex in the cavity enclosed by the deflection plates grows in size, and the size of the right vortex reduces; therefore, the four-way saddle at the vertex of the counter-rotating vortices moves toward the right direction. The issued jet tilts up a little, but it still ejects toward the upper-left direction. In Fig. 2c (t^* = 3.33), the left vortex in the cavity enclosed by the deflection plates grows continuously in size, the right vortex reduces continuously in size, and the four-way saddle at the vertex of the counter-rotating vortices moves to the right-most location. The jet issuing direction changes—it issues toward the upper-right direction, which differs from the directions observed in Figs. 2a, b. In Figs. 2d, e (t^* = 5.00 and 6.67, respectively), the right vortex in the cavity enclosed by the deflection plates grows continuously in size, and the left vortex reduces continuously in size;

therefore, the four-way saddle at the vertex of the counter-rotating vortices moves toward the left. The jet still issues toward the up-right direction, but it tilts up a little with the left movement of the four-way saddle. In Fig. 2f (t^* = 8.33), the four-way saddle moves backwards toward the right, and the jet issuing direction changes again—it issues toward the up-left direction, which is different from the directions observed in Figs. 2c–e. The left-right transversal oscillation cycle of the jet is completed. The jet oscillation proceeds continuously due to the periodic left-right movement of the four-way saddle. The oscillation frequency at the present Reynolds number Re_j = 121 is 19.6 Hz, as detected by a hot-wire anemometer that was a TSI 1210-T1.5 single-wire probe. Upon varying the jet exit flow Reynolds number, it was demonstrated that the jet oscillation frequency increases linearly as the jet Reynolds number increases. This phenomenon is akin to holding a rope at the four-way saddle and swinging the rope. When the four-way saddle moves left- and rightwards, the rope will present wave motions in the free part. The jet fluids subject to the left-right motion of the four-way saddle therefore proceed in a left-right swinging motion. The left-right swing motion of the jet column subsequently induces right-left vortical flow structures. The transverse oscillation-induced vortical flow structures break up quickly within a short axial distance. It can be seen that the jet flow widens abruptly as the vortices break up. The increase in turbulence intensity and mixing due to the increased entrainment are anticipated during the processes of jet oscillation, vortices generation, and vortices breakup. The long-exposure flow visualization image of the jet issued from the fluidic oscillator burner is shown in Fig. 3; the jet expands significantly within a short axial distance at an axial level z/d_p greater than about 0.7.

Figures 4a, b present the instantaneous and long-exposure images, respectively, of the isothermal flow patterns of the plane jet burner. The jet fluids issued from the burner exit remain coherent in the near field. The scenarios of the instantaneous (Fig. 4a and long-exposure (Fig. 4b flow patterns are similar, and the edges of the jet are relatively sharp. The jet width issued from the plane jet burner (Fig. 4) is significantly smaller than that issued from the fluidic oscillator burner (Figs. 2 and 3), implying that the transverse turbulent dispersion of the jet fluids issued from the plane jet burner is less significant than those issued from the fluidic oscillator burner. This proves that coherency is already lost, and small-scale turbulent fluctuations dominate the oscillating jet flow, unlike with the non-oscillating plane jet, where coherency extends far downstream of the jet flow.

3.2 Turbulence intensities

Figures 5a, b show the axial turbulence intensities along the central axis at various Re_j for the transversely-oscillating and non-oscillating plane jets, respectively. The data were

Fig. 2 Instantaneous flow patterns downstream fluidic oscillator burner. Jet fluid: air, $Re_j = 121$. Frame rate = 200 fps, exposure time = 2.2 ms
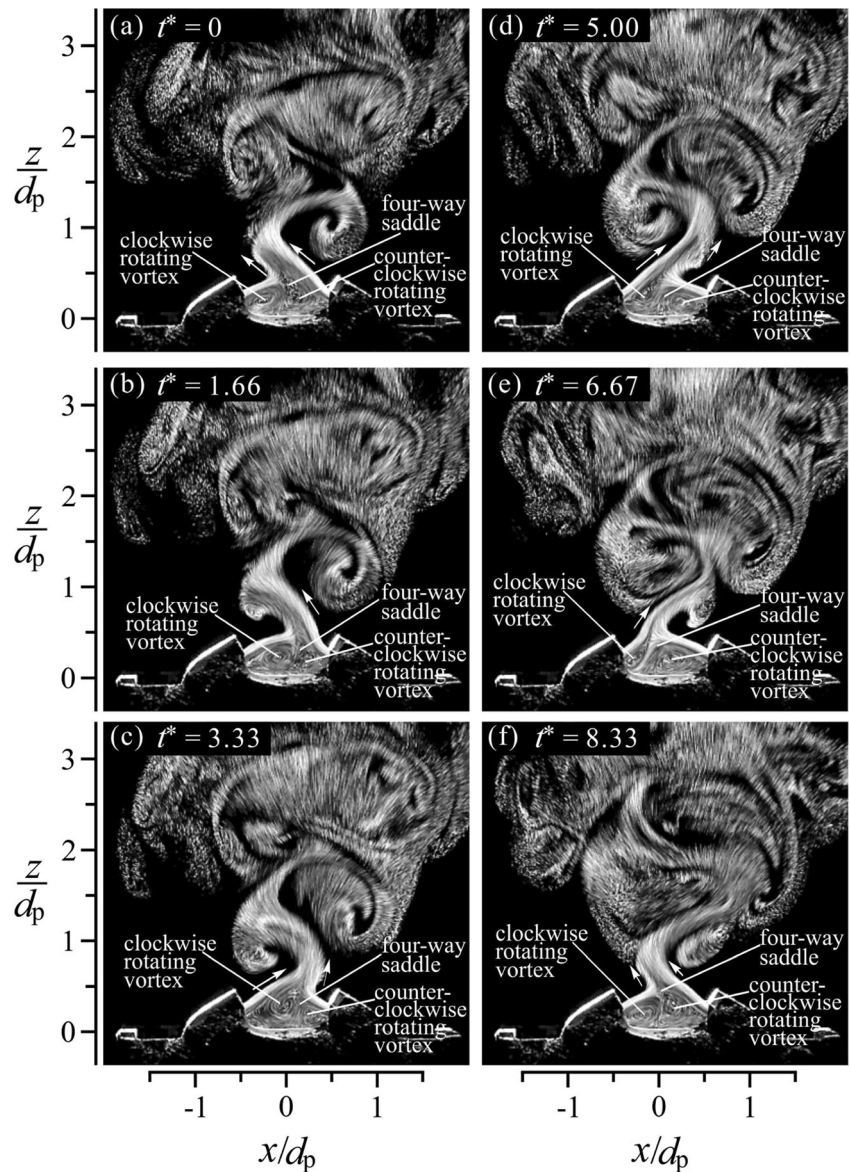
measured by a single-wire hot-wire anemometer. The axial turbulence intensity is defined as u'/u_j, where u' is the root mean square of the fluctuating velocity and u_j is the average exit velocity of the plane jet. The turbulence intensities of the transversely-oscillating jet are significantly larger than those of the non-oscillating plane jet. The turbulence intensities of the transversely-oscillating jet present near-field humps at the region $z/d_p < 2$. The peak value of the turbulence intensity escalates as the jet flow Reynolds number increases. The turbulence intensities of the non-oscillating plane jet are nearly zero at the region $z/d_p < 12$. However, for $Re_j = 423$ and 726, the turbulence intensities surge rapidly to peak values, after which they decrease gradually. For $Re_j = 726$, the values of u'/u_j are about 38% and 17% for the transversely-oscillating jet and non-oscillating plane jet, respectively. The humps presented in Fig. 5a may be associated with the stronger entrainment

of the ambient air into the transversely-oscillating jet in the near-exit region, which causes high-velocity fluctuations. The transversely-oscillating jet induces high turbulence intensities to the flow. This property has the potential of enhancing entrainment and mixing.

3.3 Flame appearance

Figure 6 shows short-exposure photographs of the transversely-oscillating jet flames around the near-exit area at various jet Reynolds numbers. The images were captured at an exposure time of 1 ms with the camera facing the y-direction. Figures 6a–c show two blue flames anchored on the tips of the deflection plates and extending downstream, with distributed blue flame all over the base and plaited-like edges— herein, plaited-like edges means that the flame edges
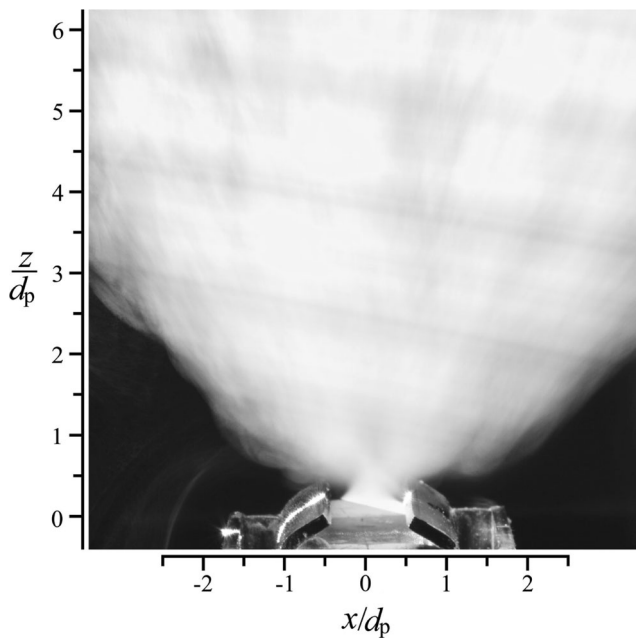
Fig. 3 Long-exposure flow pattern downstream fluidic oscillator burner. Jet fluid: air, $Re_j = 121$. Exposure time = 2.5 s

appear as if they are composed of several flame strands that have been interlaced together. In Fig. 6a, for $Re_j = 344$, the flame is attached to the tips of the deflections, and it does not fluctuate drastically. At an axial level z/d_p greater than about 0.7, the flame expands transversely with a large part of a yellow color. This type of flame appears at a Reynolds number Re_j less than about 1030, and it is termed the *attached flame*. In Fig. 6b, for $Re_j = 1204$, the blue flame bases sometimes leave and sometimes attach to the tips of the deflection plates. At an axial level z/d_p greater than about 0.7, the flame expands transversely. Downstream of the axial level of the sudden

transverse expansion of the flame, the flames fluctuate strongly with yellow and blue colours. This type of flame appears at a Reynolds number Re_j between about 1030 and 1290, and it is termed the *transitional flame*. At a jet Reynolds number Re_j higher than about 1290, the flames lift slightly above the deflection plate tips (this is not clearly visible in the images due to camera's viewing angle), and the flame fluctuations become robust, as typically shown in Fig. 6c for $Re_j = 2064$. The flames expand transversely significantly at a level of z/d_p that is higher than about 0.7, and this type of flame is termed the *lifted flame*. The axial level at which the flames expand transversely is almost the same level as that at which the isothermal jet presents a sudden expansion, as shown in Figs. 2 and 3. Above the abrupt expansion level, the flame's appearance is a mixture of yellow and blue colours with turbulent motions. The larger the Reynolds number, the more strongly the flames fluctuate. The flame width and blue flame coverage increase as the Reynolds number increases.

Figure 7 shows short-exposure photographs of the non-oscillating plane jet flames near the jet exit area at various Reynolds numbers. Although the environmental draft velocities were low, slight perturbations may exist in Fig. 7 due to a small environmental influence, especially on the low Reynolds number jet flame. The Reynolds numbers of Figs. 7a–c for the non-oscillating plane jet flames correspond to those of Figs. 6a–c for the transversely-oscillating jet flames, respectively. In Figs. 7a–c, the flames had blue edges without fluctuations, and all are attached to the burner exit, which is akin to a standard attached laminar diffusion flame. At $Re_j = 344$ (Fig. 7a), the flame is wide at the base, and it has thin-edged blue flames extending from the edges of the burner top to an axial position of $z/d_p \approx 2$, with the rest of the flame being yellowish. The wide base flame may be induced by the transverse diffusion of fuel, as the axial jet

Fig. 4 Flow patterns downstream plane jet burner. Jet fluid: air, $Re_j = 121$. (**a**) instantaneous, frame rate = 100 fps, exposure time = 2 ms, (**b**) long exposure, exposure time = 2 s
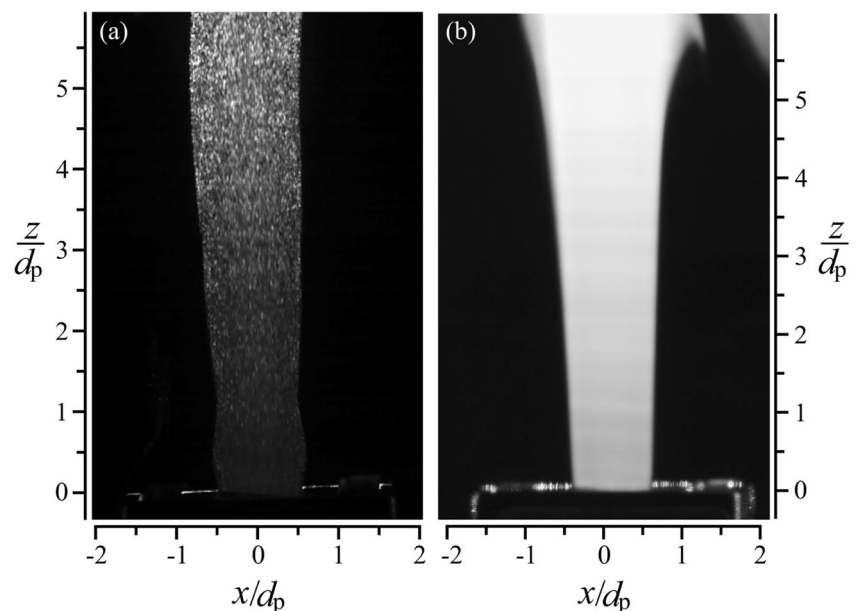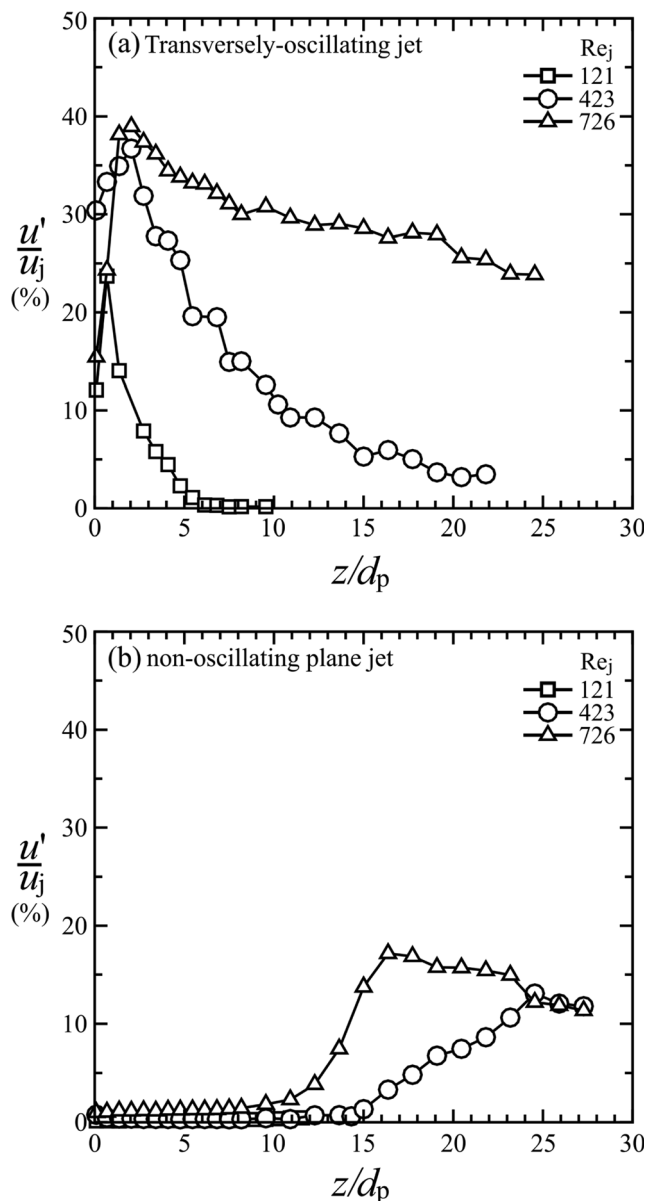
Fig. 5 Axial distributions of normalized turbulence intensities along central axis at various Re_j. (**a**) transversely-oscillating jet, (**b**) non-oscillating plane jet

Fig. 6 Typical appearances around near exit region of transversely-oscillating jet flame. Pictures taken with the camera facing y-direction. Exposure time 1 ms. (**a**) attached flame, (**b**) transitional flame, (**c**) lifted flame

momentum in this case is low. This type of flame appears at a Reynolds number Re_j of less than about 1118, and it is termed the *momentum deficit flame*. At $Re_j = 1204$ (Fig. 7b), the left blue flame base extends from the left edge of the jet exit, while the right blue flame base extends from the right edge of the burner top. The situation for the left or right anchoring of the base flames may be inverted when the experiments are repeated or when the jet Reynolds number is changed. This type of flame appears at a Reynolds number Re_j between 1118 and 1400, and it is termed the *transitional flame*. At $Re_j = 2064$ (Fig. 7c), the base blue flames reduce in width, because the base flames anchor around the edges of the jet exit. The base blue flames are located a little out of the range of the jet exit due to the characteristics of the
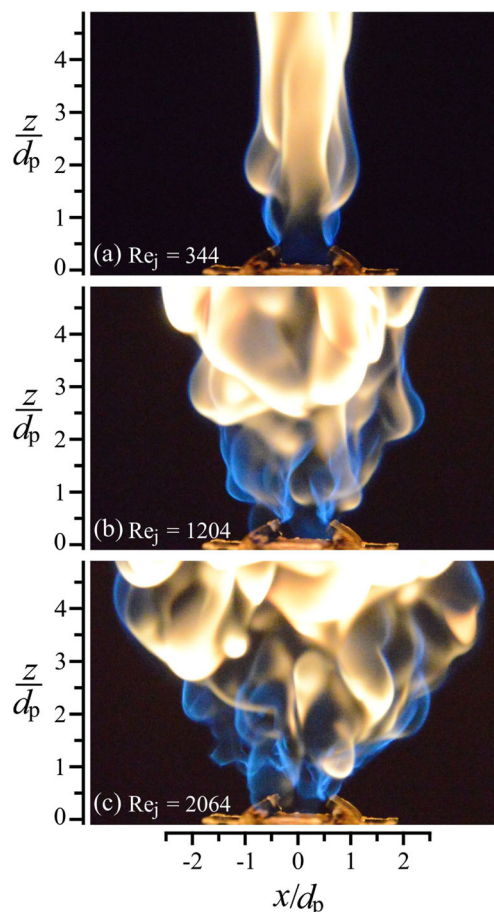
diffusion flames. This type of flame appears at a Reynolds number Re_j higher than about 1400, and it is termed the *momentum-dominated flame*. Comparing the differences between Figs. 6 and 7 at the same jet Reynolds number, it is apparent that the fluidic oscillator burner may generate wider and more turbulent flames than its corresponding plane jet burner. These differences are due to the differences in flow behaviors shown in Figs. 2, 4, and 5. The large width and strong turbulent fluctuations of the flames generated by the fluidic oscillator burner at small Reynolds numbers may be attributed to a significant entrainment and mixing ability induced by the transverse oscillations of the fuel jet.

Figures 8 and 9 exhibit long-exposure full-flame photographs at various Reynolds numbers for the transversely-oscillating jet flames and the non-oscillating plane jet flames, respectively. The time-averaged flame length and maximum flame width of both burners increase as the jet Reynolds number increases. From Figs. 8a and 9a, it is noted that for $Re_j = 344$, both flames are almost the same length. At higher Reynolds numbers of 1204 and 2064 (Figs. 8b and 9b and Figs. 8c, and 9c, respectively), the images of the transversely-oscillating jet flames appear shorter when compared to the
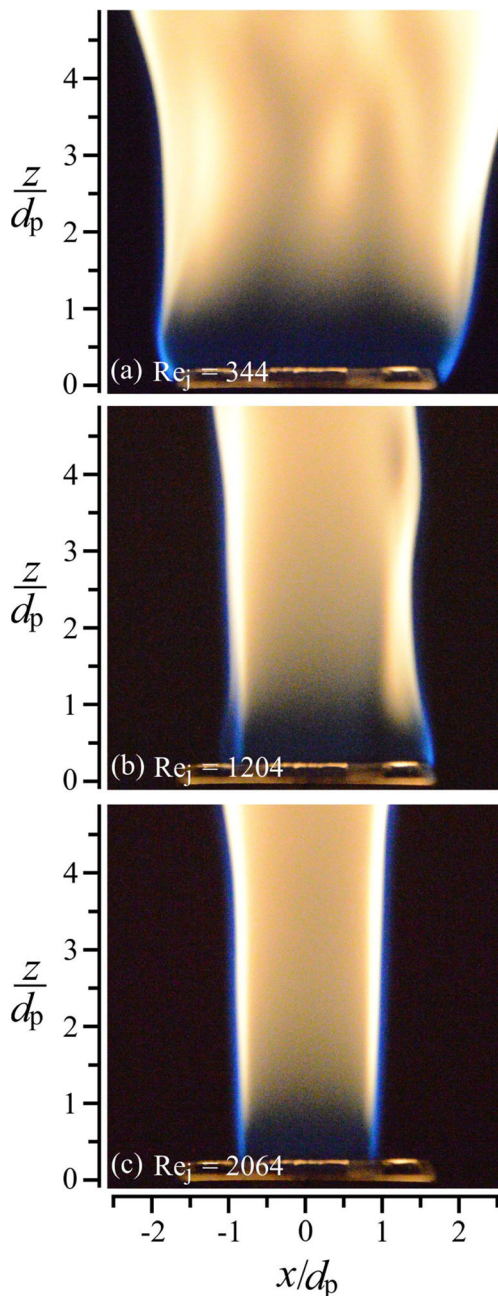
Fig. 7 Typical appearances around near exit of a non-oscillating plane jet flame. Pictures taken with camera facing *y*-direction. Exposure time 1 ms. (**a**) momentum-deficit flame, (**b**) transitional flame, (**c**) momentum-dominated flame

corresponding images of the non-oscillating plane jet flames. In the near-exit region, the widths of the transversely-oscillating jet flames are 'fatter' than their counter-part non-oscillating plane jet flames.

3.4 Flame width and length

Figure 10 shows the dimensionless flame widths in the near-exit regions of both burners at various axial levels. For the transversely-oscillating jet flames, Fig. 10a shows that the
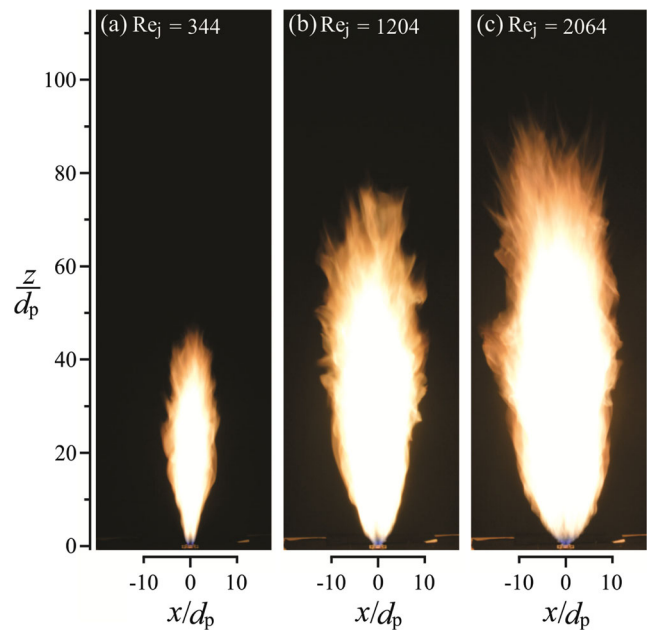

Fig. 8 Typical full-length flame appearances of transversely-oscillating jet flame. Pictures taken with the camera facing the *y*-direction. Exposure time 2 s. (**a**) attached flame, (**b**) transitional flame, (**c**) lifted flame

flame widths increase with an increasing Re_j in an almost linear manner. For the non-oscillating plane jet flames, as shown in Fig. 10b, the flame widths increase with an increasing Re_j for a small Re_j ($Re_j < 1118$) in the range of the momentum deficit flame, and it then decreases with increases of the Re_j at mediate-large values of Re_j ($1118 < Re_j < 1400$) in the range of the transitional flame. At a large Re_j ($Re_j > 1400$)
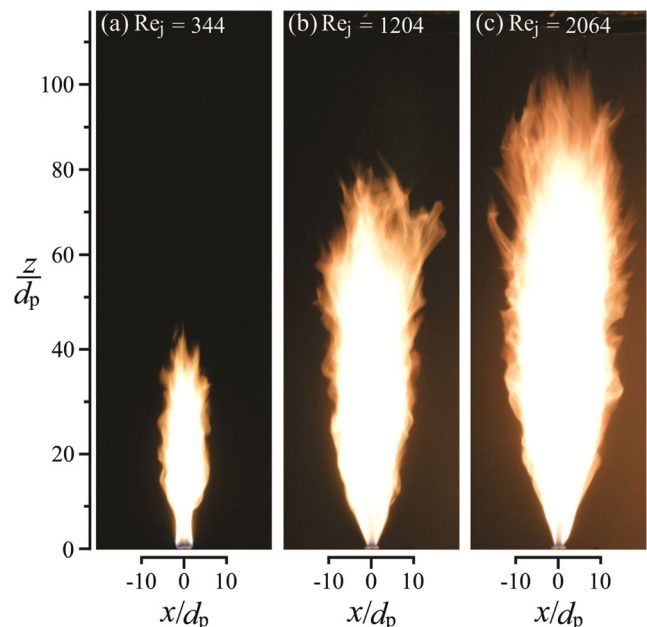

Fig. 9 Typical full-length appearances of non-oscillating plane jet flame. Pictures taken with the camera facing the *y*-direction. Exposure time 2 s. (**a**) momentum-deficit flame, (**b**) transitional flame, (**c**) momentum-dominated flame
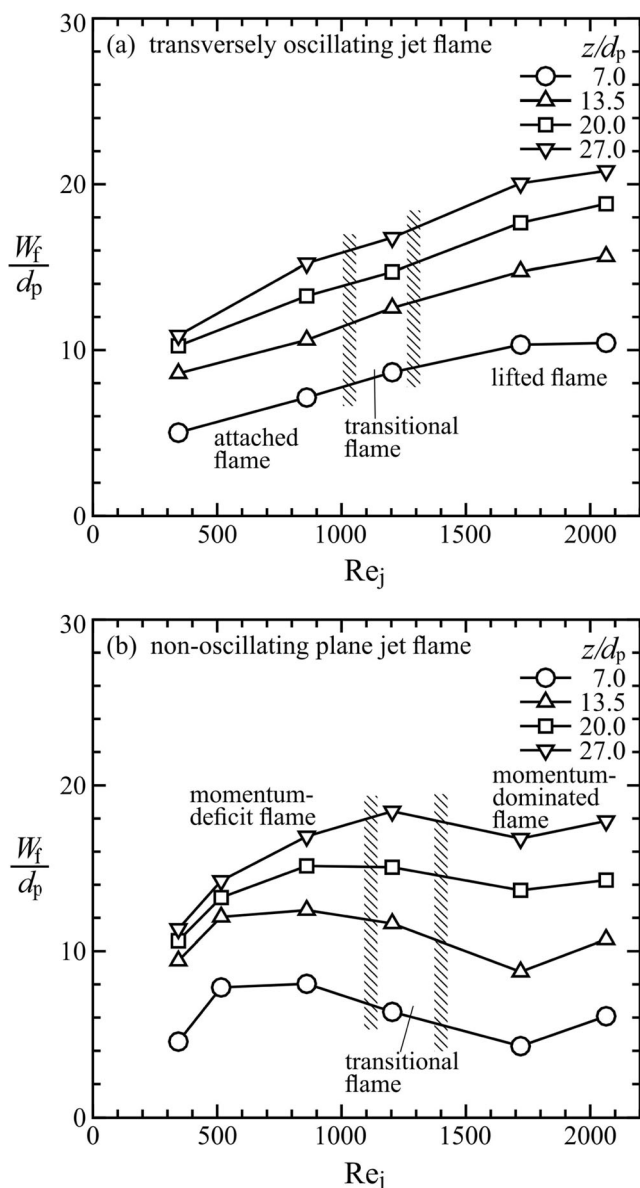
Fig. 10 Dimensionless flame widths at various axial attitudes. (**a**) transversely-oscillating jet flame, (**b**) non-oscillating plane jet flame

in the range of the momentum-dominated flame, the widths of the non-oscillating plane jet flames increase with an increasing Re_j. In the range of the momentum-dominated flame, the flame widths of the non-oscillating plane jet flames are obviously smaller than those of the transversely-oscillating jet flames. For instance, at $Re_j = 2064$, the difference compared to the non-oscillating plane jet flame width may be about 86% at $z/d_p = 7$, 48% at $z/d_p = 14$, 35% at $z/d_p = 20$, and 19% at $z/d_p = 27$. This result is in accordance with the long-exposure images shown in Figs. 8 and 9. Significant differences in the entrainment and lateral spreading rates between the transversely-oscillating jet flames and the non-oscillating plane jet flames are witnessed from the flame width trends.

Figure 11a shows the variations in the dimensionless flame length H_f/d_p with the jet Reynolds number. The lengths of the transversely-oscillating jet flames and the non-oscillating plane jet flames both increase as the jet Reynolds number increases. The lengths of the non-oscillating plane jet flames are longer than those of the transversely-oscillating jet flames. In the range of lifted flames for the transversely-oscillating jet flames, the flame lengths are significantly shorter than those of the momentum-dominated flame for the non-oscillating plane jet flames. At $Re_j = 2064$, the difference compared to the non-oscillating plane jet flame length may reach about 20%. When regressed, the measured flame lengths presented in Fig. 11a give seventh power polynomial formulas, which are capable of predicting the flame lengths for the jet Reynolds numbers $Re_j \leq 2400$. For the transversely-oscillating jet flames:

$$
\begin{aligned}
\frac{H_f}{d_p} = \ & -1.2 \times 10^{-1} + 2.64 \times 10^{-1} Re_j \\
& -5.11 \times 10^{-4} Re_j^2 + 6.05 \times 10^{-7} Re_j^3 \\
& -4.13 \times 10^{-10} Re_j^4 + 1.59 \times 10^{-13} Re_j^5 \\
& -3.16 \times 10^{-17} Re_j^6 + 2.47 \times 10^{-21} Re_j^7
\end{aligned} \tag{1}
$$

For the non-oscillating plane jet flames:

$$
\begin{aligned}
\frac{H_f}{d_p} = \ & -3.48 + 3.03 \times 10^{-1} Re_j \\
& -6.83 \times 10^{-4} Re_j^2 + 9.6 \times 10^{-7} Re_j^3 \\
& -7.63 \times 10^{-10} Re_j^4 + 3.4 \times 10^{-13} Re_j^5 \\
& -7.93 \times 10^{-17} Re_j^6 + 7.52 \times 10^{-21} Re_j^7
\end{aligned} \tag{2}
$$

The maximum deviations of the regressed values using Eqs. (1) and (2) from the measured values were 1.26% and 2.31%, respectively.

Figure 11b presents the slopes for the flame length growth curves, which are obtained from the derivatives of Eqs. (1) and (2) with respect to Re_j. Steep variations in the length derivatives are found between $Re_j = 170$ and $Re_j = 600$. However, the variations in length derivatives attain an almost constant value for each Reynolds number at $Re_j > 1400$, meaning that at high Reynolds numbers, the fuel jet Reynolds number has lesser influence on flame length. The change in slope appearing at the range $800 < Re_j < 1400$ in Fig. 11b may indicate the boundaries for the flame regimes marked in Fig. 11. For the transversely-oscillating jet flames, the constant flame length growth rate is about 0.0182, while the non-oscillating plane jet flames have a constant flame length growth rate of about 0.0294, which is almost 1.5 times higher. The lengths increase at a higher rate with an increasing Re_j for the attached flame of the transversely-oscillating jet flames and for the momentum deficit flame of the non-oscillating plane jet flames. The large flame length growth rate observed for the plane jet burner as compared to the fluidic oscillator burner is attributed to the poor mixing and
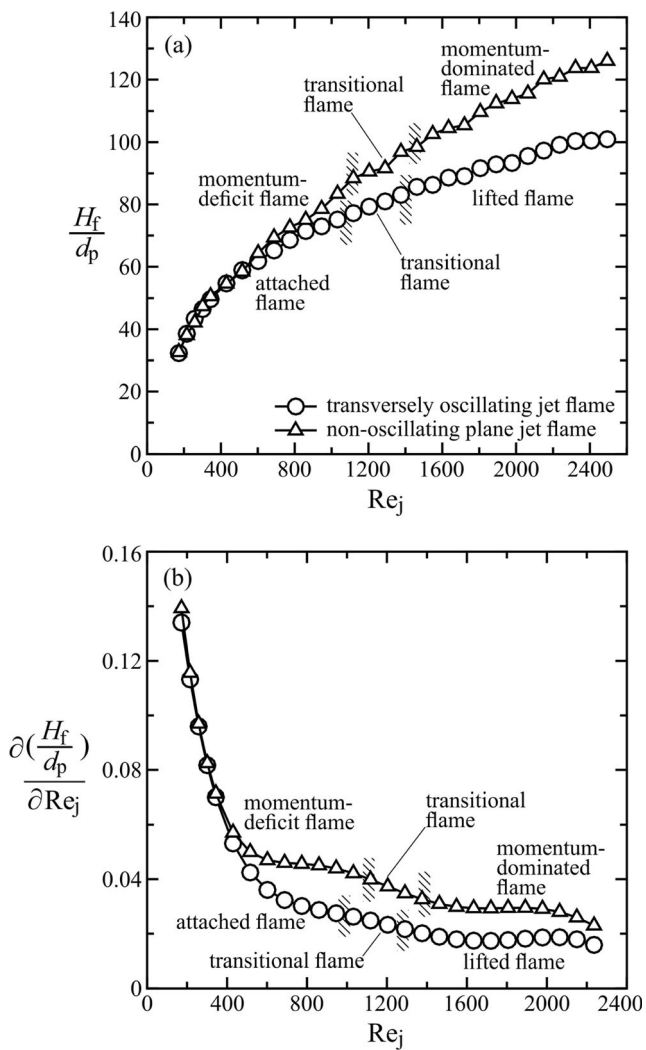
Fig. 11 Characteristics of flame lengths. (**a**) dimensionless flame length, (**b**) change rate of dimensionless flame length with jet Reynolds number

entrainment of the plane jet burner flame, mostly at the near field to the burner exit which is believed to have slowed the combustion process.
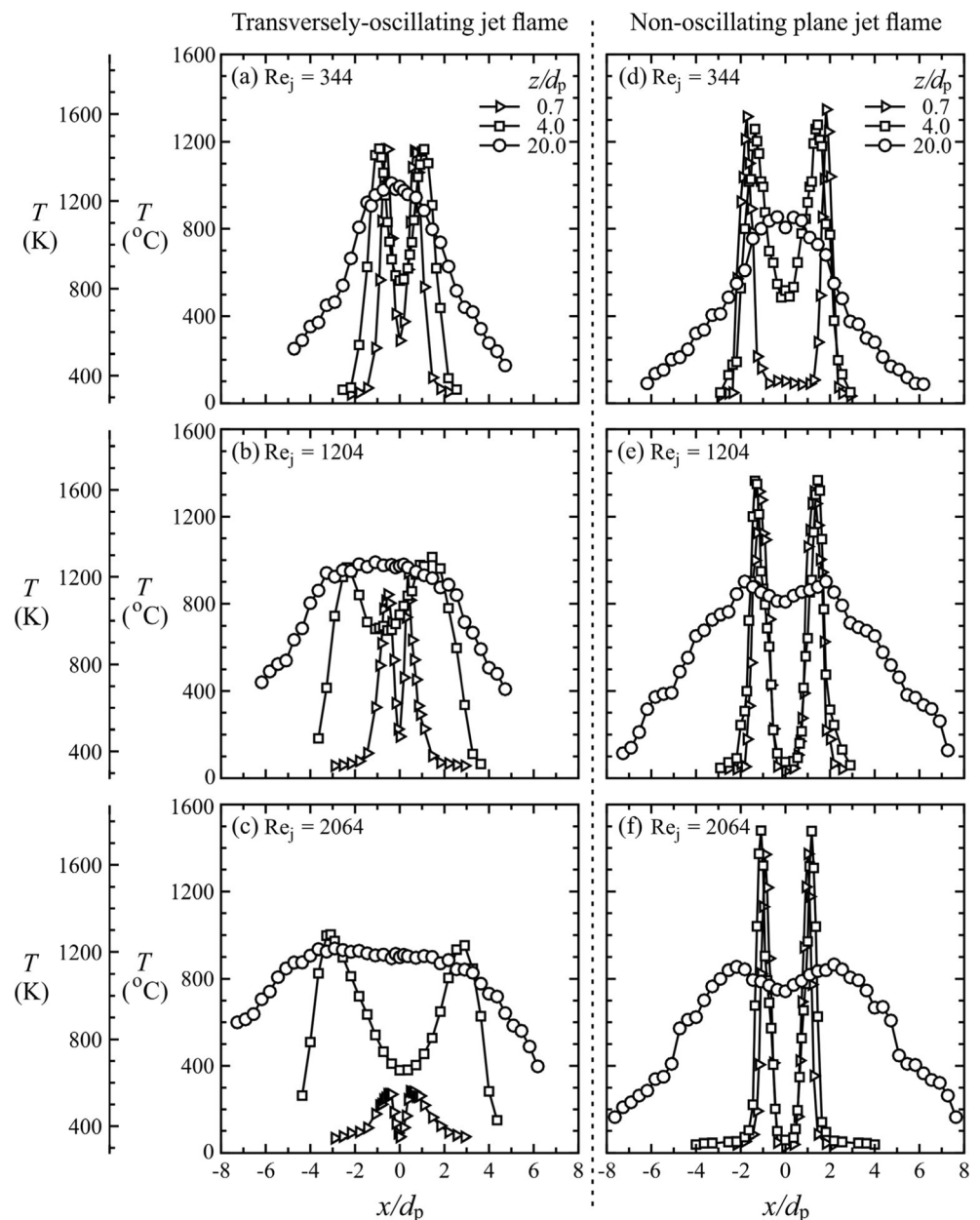
3.5 Temperature distributions

Figure 12 shows the transverse temperature distributions at various axial levels of the transversely-oscillating and non-oscillating plane jet flames at various jet Reynolds numbers. Figures 12a–c show the transverse temperature distributions at various axial levels of the transversely-oscillating jet flames. For all flame modes, the temperature distributions at low axial levels $z/d_p = 0.7$ and 4.0 present twin-peak patterns, but they turn to a Gaussian-like distribution at high axial levels $z/d_p = 20$. At $Re_j = 344$ for the attached flame, as in Fig. 12a, the peaks have values of 1180 °C at $x/d_p \approx \pm 1.1$ for the axial levels $z/d_p = 0.7$ and 4.0. At $z/d_p = 20$, the temperature profile becomes Gaussian-like with a maximum temperature of

1020 °C. Figure 12b presents the temperature distributions for the transitional flame. The temperatures at the twin peaks of the axial levels $z/d_p = 0.7$ and 4.0 are 860 °C (at $x/d_p \approx \pm 0.7$) and 1050 °C (at $x/d_p \approx \pm 2$), respectively. The transitional flame temperature distribution at $z/d_p = 20$ has a Gaussian-like profile, with a maximum temperature of approximately 1000 °C. In Fig. 12c for the lifted flame, the temperatures at $z/d_p = 0.7$ are low due to the lack of flames. The twin-peak temperature distribution appears at the axial level $z/d_p = 4.0$, with a maximum temperature of about 1000 °C at $x/d_p \approx \pm 3.0$. At the axial level $z/d_p \approx 20.0$, a plateau-like temperature distribution extending from $x/d_p = -3.8$ to 3.5 with a maximum temperature of 920 °C is obtained.

Figures 12d–f show the temperature distributions at various axial levels of the non-oscillating plane jet flames at various jet Reynolds numbers. All temperature profiles display twin-peak patterns, which are a feature of diffusion flames. In Fig. 12d, for the momentum deficit flame, a peak temperature of 1320 °C appears at $x/d_p \approx \pm 1.6$ at the axial level $z/d_p = 0.7$. At the axial level $z/d_p = 4.0$, a peak temperature of 1260 °C is observed at $x/d_p \approx \pm 1.4$. The valley temperatures around the center region of the axial levels $z/d_p = 0.7$ and 4.0 present relatively low values when compared with the corresponding cases shown in Fig. 12a. A peak temperature of 860 °C at the axial level $z/d_p = 20$ (Fig. 12d) is observed at $x/d_p \approx \pm 0.4$. Compared with Fig. 12a, a transversely-oscillating jet flame at $z/d_p = 4.0$ has evolved into a Gaussian-like profile; the corresponding non-oscillating plane jet flame at the same axial level, however, still presents a twin-peak feature. In Figs. 12e, f for the transitional and momentum-dominated flames, respectively, the twin-peak feature at $z/d_p = 4.0$ and the low valley temperatures around the center region at the axial levels of $z/d_p = 0.7$ and 4.0 are similar to those shown in Fig. 12d, which indicates the characteristics of a laminar diffusion flame. The peak temperatures at the axial level of $z/d_p = 20.0$ in Figs. 12e, f are 900 °C and 860 °C, respectively, which are apparently lower than the maximum temperatures of 1050 °C and 1000 °C of the plateau-like distributions in Figs. 12b, c, respectively.

Comparing the temperature distributions of the transversely-oscillating jet flame and non-oscillating plane jet flame shown in Figs. 12a–f, respectively, it is noted that the non-oscillating plane jet flame produces higher peak temperatures at low axial levels of $z/d_p = 0.7$ and 4.0 due to the characteristics of the diffusion flame. However, because of the characteristics of the partially premixed flame induced by the enhanced entrainment and mixing due to the transverse oscillation of the fuel jet, the transversely-oscillating jet flame exhibits higher and wider Gaussian peaks at $z/d_p = 20$ for all Reynolds numbers sampled. Considering the temperature distributions at $z/d_p = 20$ and the corresponding flame widths and lengths, it is evident that the transversely-oscillating jet flame indicates a greater combustion efficiency. The non-oscillating

Fig. 12 Transverse temperature distributions at various altitudes. (**a**)-(**c**) transversely-oscillating jet flames (**d**)-(**f**) non-oscillating plane jet flames. (**a**) attached flame, (**b**) transitional flame, (**c**) lifted flame (**d**) momentum-deficit flame, (**e**) transitional flame, (**f**) momentum-dominated flame

plane jet flame has higher peak temperatures at low axial levels of z/d_p due to the poor mixing near the burner exit. The slightly lower temperatures at lower axial levels of the transversely-oscillating jet flame are induced by large entrainment and mixing rates, because the entrained air lowers the flame temperatures.

Figure 13 shows the axial temperature distributions along the central axis of the two burners investigated. The axial temperatures increase to a maximum and then decrease. This divides the flame into three parts: a growing section, a peak, and a decreasing section. When compared with Fig. 13b, it is observed in Fig. 13a that the growth sections are steeper, the peaks are slightly higher, and the decreasing regions are slightly sloppy. Considering the shape of the axial temperature

distributions, there exists a critical axial level that divides the flame into two regions. The two distinctive regions were termed the *reaction-dominated zone* (the temperature growth section) and the *convection-dominated zone* (the temperature decreasing section), respectively [29]. As seen in Figs. 13a, b, at $Re_j = 344$, the reaction-dominated zones are almost equal; this confirms the overlapping of the flame lengths for $Re_j < 600$, as noted in section 3.4, which implies that the combustion performances of the two burners investigated are comparable at low jet Reynolds numbers ($Re_j < 600$). However, in Fig. 13a at a high Re_j, the temperatures in the reaction-dominated zones are larger in comparison to those appearing in Fig. 13b. This implies that at large jet Reynolds numbers, the transversely-oscillating jet flame presents a combustion
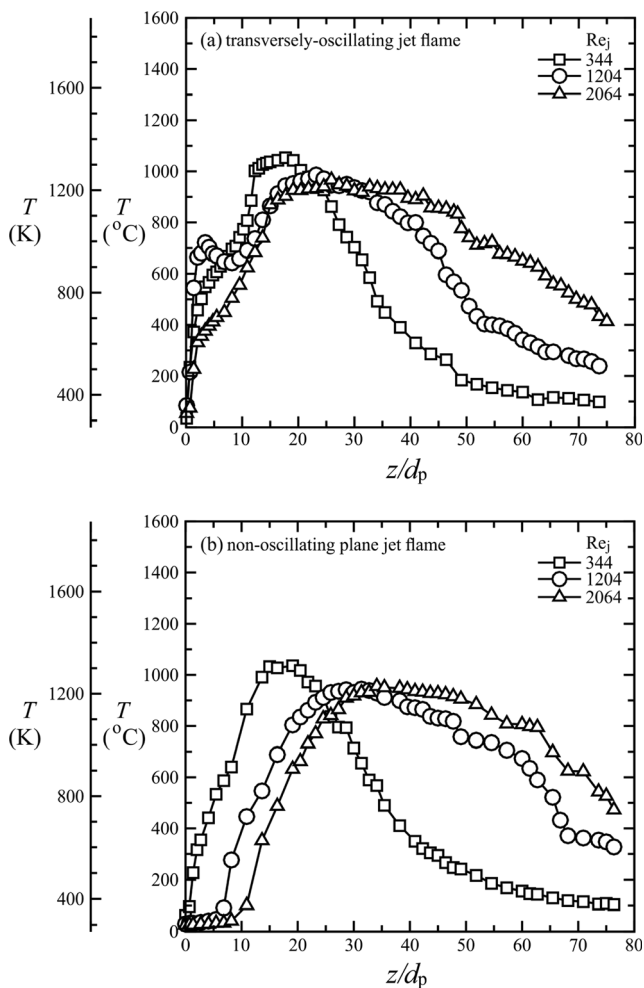
Fig. 13 Temperature distributions along central axis. (**a**) transversely-oscillating jet flame, (**b**) non-oscillating plane jet flame

performance superior to the non-oscillating plane jet flame. This explains the role of transverse oscillations in entrainment and mixing.

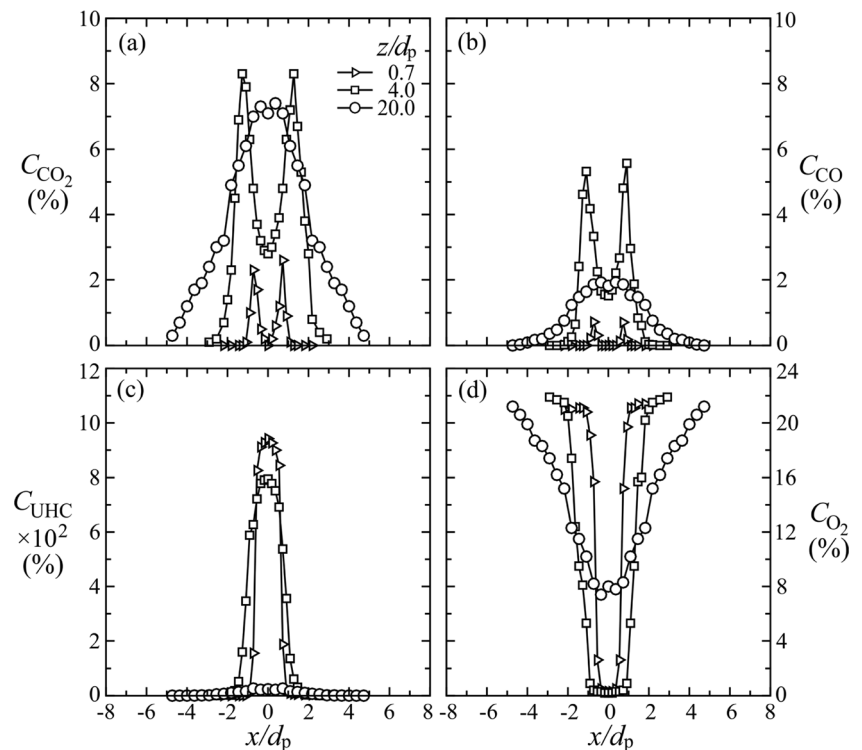### 3.6 Combustion product concentrations

Figures 14 and 15 show the lateral distributions of combustion product concentrations at $Re_j = 344$ for the transversely-oscillating jet flame and the non-oscillating plane jet flame, respectively. Both figures show concentrations of CO_2, CO, UHC, and O_2 at three axial levels. Figures 14a and 15a show twin-peak distributions of CO_2 at lower axial levels and a single-hump profile at high axial levels. The CO_2 concentrations of the transversely-oscillating jet flame have higher values than those of the non-oscillating plane jet flame. The CO concentration distributions in Figs. 14b and 15b have similar shapes to those shown in Figs. 14a and 15a for CO_2 concentration distributions, but the peak values are lower than those of the CO_2 concentrations. At $z/d_p = 0.7$ and 4.0, the CO concentration distributions in Figs. 14b and 15b show dual-

peak profiles, which indicates diffusion flames. The transversely-oscillating and non-oscillating jet flames at a lower axial level register insignificant CO emissions compared to those at higher axial levels. The profiles at $z/d_p = 4.0$ show higher peaks for the transversely-oscillating jet flame, and this may be understood to be a result of the entrainment of cold air by the transversely-oscillating fuel jet, which cools the hot combustion gases, hence retarding the reaction process. At $z/d_p = 20.0$, the CO concentration distributions of the transversely-oscillating and non-oscillating jet flames turn to Gaussian-like profiles. The peak values at $z/d_p = 20.0$ are lower than those at $z/d_p = 4.0$ because of the merging of the diffusion flames. The transversely-oscillating jet flame produces a large transverse dispersion; therefore, the CO distribution of the transversely-oscillating flame is wider than that of the non-oscillating jet flame. The distributions of the UHC shown in Figs. 14c and 15c denote almost zero values at $z/d_p = 20$. However, the UHC profiles at $z/d_p = 0.7$ and 4.0 of Fig. 15c for the plane jet burner flame present slightly larger maximum values and 'fatter' distributions around the central part of the flame when compared with those of the corresponding transversely-oscillating jet flame. This indicates that the combustion occurring in the transversely-oscillating jet flame is more complete than that which occurs in the non-oscillating plane jet flame. Figures 14d and 15d show the O_2 concentration distributions within the transversely-oscillating jet flame and the non-oscillating plane jet flame, respectively. The O_2 diffuses from the ambient environment into the flame. At $z/d_p = 20$, the O_2 profile for Fig. 14d is wider than that for Fig. 15d due to the enhanced entrainment effect occurring in the transversely-oscillating jet flame. The transversely-oscillating jet flames present characteristics of partially premixed flames, particularly at high values of Re_j. This is an indicator of the role of the transverse oscillation phenomenon in entrainment, axial momentum dispersion, and fuel-air mixing ability. The Damköhler number (Da) represents the ratio of a chemical reaction rate to the diffusion rate of fuel and air. Because the turbulence intensities in the flow of the transversely-oscillating jet are significantly increased when compared with those of the non-oscillating jet, the Damköhler number is decreased. Therefore, the combustion rate is increased. The non-oscillating plane jet flame exhibits the behavior of diffusion flames that occurs when the mixing rate is much slower than the combustion reaction rate (Da >1).

4 Conclusions

A fluidic oscillator burner installed with deflection plates was developed together with a plane jet burner and used in this study. Comparisons were made between the near-field flow and flame images, flame widths, flame lengths, temperatures,

Fig. 14 Combustion product concentration distributions of transversely-oscillating jet flame. $Re_j = 344$. (a) carbon dioxide, (b) carbon monoxide, (c) unburned hydrocarbon, (d) oxygen


and combustion product concentration distributions. The following conclusions were drawn from the results of the study.

(1) The installation of deflection plates on the top of the fluidic oscillator burner induced the merging of

bifurcated jets issuing alternately from the fluidic oscillator, therefore generating a transversely-oscillating jet. The transverse oscillations of the merged jet transferred the axial jet momentum into periodic vortical flow motions and high turbulent fluctuations, thereby inducing

Fig. 15 Combustion product concentration distributions of non-oscillating plane jet flame. $Re_j = 344$. (**a**) carbon dioxide, (**b**) carbon monoxide, (**c**) unburned hydrocarbon, (**d**) oxygen
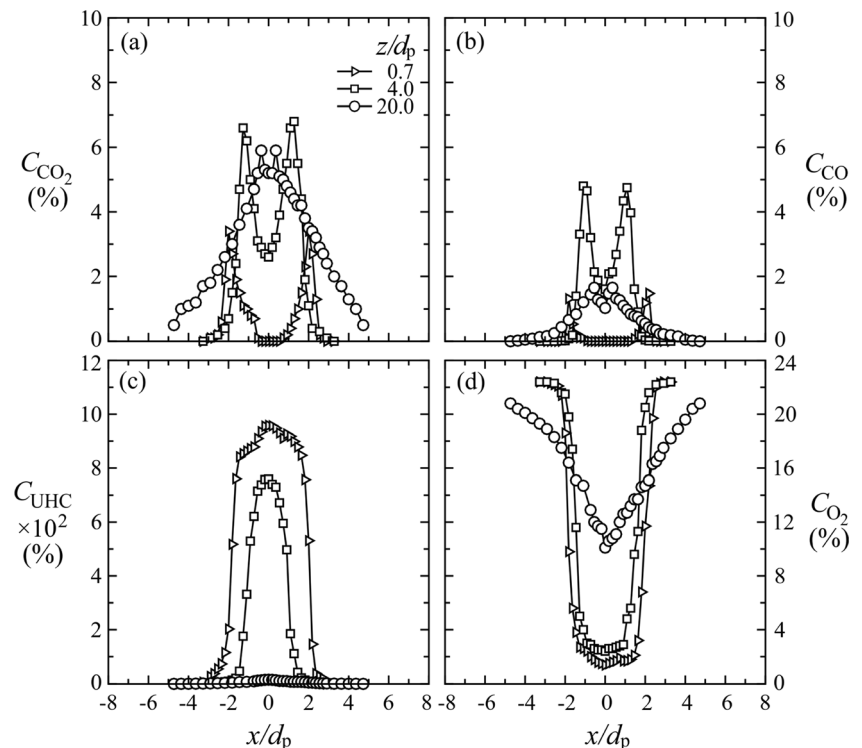
an abrupt lateral expansion of the jet fluids in the near-exit region, which indicated an enhancement in entrainment and mixing.

(2) The transversely-oscillating jet flames presented turbulent appearances, even at low Reynolds numbers, and they had wider and shorter appearances than those of the non-oscillating plane jet flames, particularly at high jet Reynolds numbers. The difference in flame width compared to the non-oscillating plane jet flame width at $Re_j = 2064$ might be about 86% at $z/d_p = 7$, while the difference in flame length compared to the non-oscillating plane jet flame length at $Re_j = 2064$ might be about 20%.

(3) The non-oscillating plane jet flames presented higher peak temperatures at low axial levels due to the characteristics of the diffusion flame. The transversely-oscillating jet flames portrayed higher and wider Gaussian peaks at high axial levels because of the characteristics of the partially premixed flame induced by enhanced entrainment and mixing due to the transverse oscillation of the fuel jet. At large jet Reynolds numbers, the transversely-oscillating jet flames presented a superior combustion performance than the non-oscillating plane jet flames.

(4) The transversely-oscillating jet flames had larger CO_2 concentrations and smaller UHC concentrations than the non-oscillating plane jet flames, indicating that the combustion process that occurred in the transversely-oscillating jet flames was more complete than that in the non-oscillating plane jet flames. The transverse oscillations of the fuel jet enhanced entrainment and mixing in the flow field by forming vortical motions and turbulence, thereby improving combustion performance.

Compliance with ethical standards

References

1. Gordeyev SV, Thomas FO (2002) Coherent structure in the turbulent planar jet. part 2. Structural topology via POD eigenmode projection. J Fluid Mech 460:349–380. https://doi.org/10.1017/S0022112002008364

2. Landel JR, Caulfield CP, Woods AW (2012) Meandering due to large eddies and the statistically self-similar dynamics of quasi-two-dimensional jets. J Fluid Mech 692:347–368. https://doi.org/10.1017/jfm.2011.518

3. Manivannan P, Sridhar BTN (2013) Characteristic study of non-circular incompressible free jet. Therm Sci 17(3):787–800. https://doi.org/10.2298/TSCI110208116M

4. Mi J, Nathan GJ (2010) Statistical properties of turbulent free jets issuing from nine differently-shaped nozzles. Flow Turbulence Combust 84:583–606. https://doi.org/10.1007/s10494-009-9240-0

5. Wygnanski BI, Fiedler H (1969) Some measurements in the self-preserving jet. J Fluid Mech 38(part 3):577–612

6. Coles D (1985) The use of coherent structures. AIAA Paper 1985–0506

7. Brown GL, Roshko A (1974) On density effects and large structure in turbulent mixing layers. J Fluid Mech 64(part 4):775–816

8. Koched A, Pavageau M, Aloui F (2011) Vortex structure in the wall region of an impinging plane jet. Journal of Applied Fluid Mechanics 4(2, Special Issue):61–69

9. Chang KT, Huang RF (2004) Development and characterization of jet-injected vee-gutter. J Mech 20(1):77–83

10. Huang RF, Chang KT (2005) Fluidic oscillation influences on v-shaped bluffbody flow. AIAA J 43(11):2319–2328. https://doi.org/10.2514/1.13604

11. Huang RF, Chang KT (2007) Evolution and turbulence properties of self-sustained transversely oscillating flow induced by fluidic oscillator. J Fluids Eng 129(8):1038. https://doi.org/10.1115/1.2746905

12. Mataoui A, Schiestel R (2009) Unsteady phenomena of an oscillating turbulent jet flow inside a cavity: Effect of aspect ratio. Journal of Fluids and Structures 25:60–79. https://doi.org/10.1016/j.jfluidstructs.2008.03.010

13. Mi J, Nathan GJ (2004) Self-excited jet-precession strouhal number and its influence on downstream mixing field. Journal of Fluids and Structures 19(6):851–862. https://doi.org/10.1016/j.jfluidstructs.2004.04.006

14. Wong CY, Nathan GJ, O'Doherty T (2004) The effect of initial conditions on the exit flow from a fluidic precessing jet nozzle. Exp Fluids 36:70–81. https://doi.org/10.1007/s00348-003-0642-9

15. Tomac MN, Gregory JW (2014) Internal flow physics of a fluidic oscillator in the transition regime. Active Flow & Combustion Control AFCC 2014 (Berlin 2014)

16. Sun C-L, Sun C-Y (2011) Effective mixing in a microfluidic oscillator using an impinging jet on a concave surface. Microsyst Technol 17:911–922. https://doi.org/10.1007/s00542-010-1177-7

17. Tesař V, Smyk E, Peszynski K (2014) Fluidic oscillator with bistable turn-down amplifier. Colloquium Fluid Dynamics 2014: 1–14. https://doi.org/10.13140/2.1.1702.1448

18. Yang J-T, Chen C-K, Hu I-C, Lyu P-C (2007) Design of a self-flapping microfluidic oscillator and diagnosis with fluorescence methods. J Microelectromech Syst 16(4):826–835. https://doi.org/10.1109/JMEMS.2007.899338

19. Gregory JW, Sullivan JP, Raman G, Raghu S (2004) Characterization of a micro fluidic oscillator for flow control. 2nd AIAA Flow Control Conference AIAA 2004–2692

20. Yang J-T, Chen C-K, Tsai K-J, Lin W-Z, Sheen H-J (2007) A novel fluidic oscillator incorporating step-shaped attachment walls. Sensors Actuators A 135:476–483. https://doi.org/10.1016/j.sna.2006.09.016

21. Deo RC, Mi J, Nathan GJ (2007) The Influence of nozzle aspect ratio on plane jets. Exp Thermal Fluid Sci 31(8):825–838. https://doi.org/10.1016/j.expthermflusci.2006.08.009

22. Kalghatgi GT (1984) Lift-off heights and visible lengths of vertical turbulent jet diffusion flames in still air. Combust Sci Technol 41: 17–29. https://doi.org/10.1080/00102208408923819

23. Peters N, Williams FA (1983) Liftoff characteristics of turbulent jet diffusion flames. AIAA J 21(3):423–429

24. Chung SH, Lee BJ (1991) On the characteristics of laminar lifted flames in a nonpremixed jet. Combustion and Flame 86:62–72

25. Iyogun CO, Birouk M (2008) Effect of fuel nozzle geometry on the stability of a turbulent jet methane flame. Combust Sci Technol 18(12):2186–2209. https://doi.org/10.1080/00102200802414980

26. Huang RF, Chang KT (2004) Oscillation frequency in wake of a vee gutter. J Propuls Power 20(5):871–878. https://doi.org/10.2514/1.9431

27. Huang RF, Yang HF, Hsu CM (2012) Flame behavior and thermal structure of combusting nonpulsating and pulsating plane jets. J Propuls Power 29(1):114–124. https://doi.org/10.2514/1.B34580

28. Yang HF, Hsu CM, Huang RF (2014) Flame behavior of bifurcated jets in a v-shaped bluff-body burner. J Mar Sci Technol 22(5):606–611. https://doi.org/10.6119/JMST-013-1025-1

29. Yang HF, Hsu CM, Huang RF (2014) Controlling Plane-Jet Flame by a Fluidic Oscillation Technique. J Eng Gas Turbines Power 136(041501):1–10. https://doi.org/10.1115/1.4025928

30. Glassman I, Yetter RA (2008) Combustion. Fourth edn. Elsevier Inc., London